REVIEW

Progress of Nb-containing catalysts for carbon dioxide reduction: a minireview

Jun-Xian Gao[1,2] · Wen-Jie Tian[2] · Hua-Yang Zhang[2]

Abstract

Nb-containing catalysts have the potential to catalyze carbon dioxide (CO_2) reduction due to their strong surface acidity and CO_2 activation sites. Still, they have not been widely used in the development and design of catalysts due to the theoretical/cost/safety limitations. Related advances have been continuously reported in the literature, demonstrating to some extent the promise of catalytic applications of Nb-containing catalysts in this area. In this minireview, we discuss the structure–activity relationships of Nb-containing catalysts for photo-, electro-, and thermocatalytic reduction of CO_2. The engineering strategies of Nb-containing catalysts for enhancing the conversion and selectivity of CO_2 reduction are discussed, ranging from Nb doping, noble metal decoration, surface acidity adjustment, oxygen vacancy engineering, and heterojunction construction to Nb or Nb_2O_5 particle decoration. The theoretical calculation research for the possible reaction paths and product selectivity is also discussed. Finally, the prospects for designing and optimizing Nb-containing catalysts are proposed. With a deep understanding of catalytic activity and reaction mechanism, this minireview is expected to present the optimization of the Nb-containing catalysts for efficient and highly selective CO_2 reduction.

Keywords Niobium · Carbon dioxide reduction · Photocatalysis · Electrocatalysis · Thermocatalysis

1 Introduction

The reduction of carbon dioxide into fuels [1] (e.g., CO, CH_4, CH_3OH, CH_3H_2OH) or other high-value products [2] (e.g., HCOOH, CH_3CHO, C_2H_4) is a feasible way to alleviate energy crisis and global warming [3]. CO_2 can be reduced through electrocatalysis [4], photocatalysis [5], and thermocatalysis [6]. The catalytic pathway can be typically divided into four steps [7]: (i) adsorption of CO_2 on the active sites of the catalyst surface; (ii) CO_2 activation (increasing C=O bond strength or bending CO_2 molecule; (iii) hydrogenation, deoxygenation, and carbon–carbon coupling of adsorbed CO_2; (iv) desorption of reduction products. The first two steps are typically identified as

rate-determining steps of CO_2 reduction, while the product selectivity highly depends on the third and fourth steps.

Nb-based catalysts have been applied in CO_2 reduction benefiting from their strong surface acidity [8], nontoxicity [9], low cost, high mechanical stability, and excellent redox stability [10]. During CO_2 reduction, the strong surface acidity favors the formation of carbon-based intermediates, such as bidentate carbonates, monodentate carbonates, and bicarbonates [11]. In addition, Nb could act as the dopant to adjust the electronic structure of the matrix materials to promote CO_2 reduction by optimizing each step, such as enhancing CO_2 adsorption [12, 13], accelerating CO_2 hydrogenation [14] and promoting CO desorption [15]. Many researchers have reported Nb-based catalysts for CO_2 reduction under different catalytic driving forces, but few reviews have summarized the structure–activity relationship of such catalysts. Herein, this minireview summarizes the applications, structure–activity relationship, and theoretical calculation studies of Nb-containing catalysts for the photo-, electro-, and thermocatalytic reduction of CO_2. Different structure engineering procedures, including Nb doping, noble metal decoration, surface acidity adjustment, oxygen vacancy engineering, heterojunction building, and Nb or

✉ Wen-Jie Tian
  wenjie.tian@adelaide.edu.au

✉ Hua-Yang Zhang
  huayang.zhang@adelaide.edu.au

1 School of Environment and Civil Engineering, Jiangnan University, Wuxi 214122, China

2 School of Chemical Engineering and Advanced Materials, The University of Adelaide, Adelaide, SA 5005, Australia
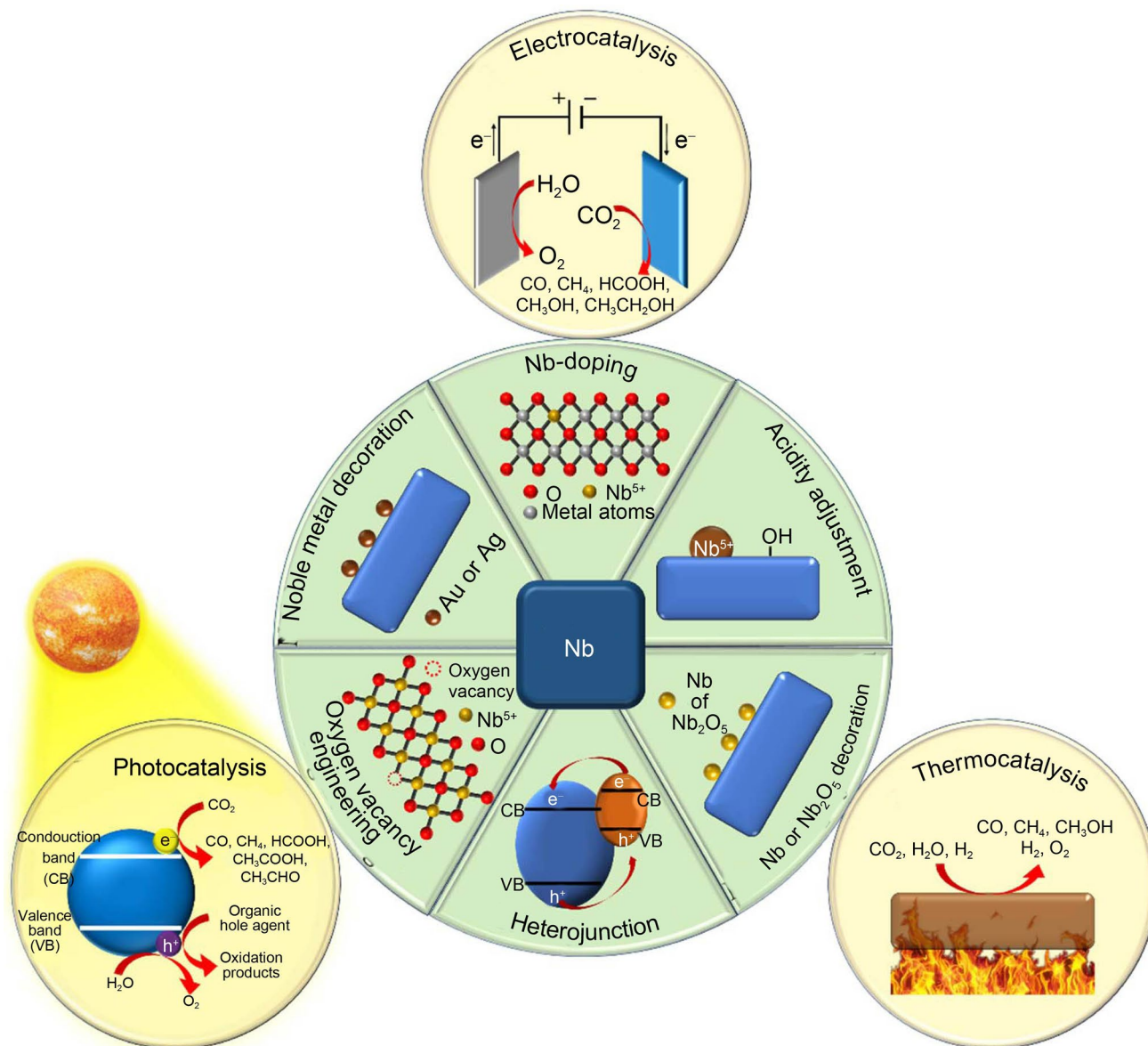
Fig. 1 Schematic illustration of engineering strategies on Nb-containing catalysts for CO_2 reduction

Nb_2O_5 particle decorating, are also addressed for performance increase (Fig. 1). Finally, the advantages, limitations, and feasible future development directions of Nb-containing catalysts for CO_2 reduction are outlined.

2 Photocatalytic CO_2 reduction

Photocatalytic CO_2 reduction is a green catalytic technology with low-energy consumption and no secondary pollution [16]. Under irradiation, photoexcited electrons from the conduction band (CB) of semiconductor-based photocatalysts reduce the adsorbed CO_2 to produce CO, CH_4, HCOOH, etc. [17]. Depending on the number of

transferred electrons and the reduction potential of different intermediates [18, 19], CO_2 reduction to different products is summarized in Table 1. The redox capacity of the catalysts, the adsorption–desorption, and the activation behavior of CO_2 on the surface of the catalysts can impact the yield and selectivity of CO_2 reduction products [20, 21]. Therefore, selecting or engineering an appropriate photocatalyst for the desired reduction products is important. Niobium-based photocatalysts currently used for CO_2 reduction include Nb–TiO_2 [22, 23], Nb_2O_5 [24], HNb_3O_8 [25], Nb-based perovskites [26], and Nb-containing high-entropy nitrides [27].

Table 1 Standard electrochemical potentials for reducing CO_2 into different products

CO_2 reduction reaction	E^0 (V) vs. SHE[a] at pH 7	References
$CO_2 + e^- \rightarrow CO_2^-$	− 1.90	[18]
$CO_2 + 2H^+ + 2e^- \rightarrow HCOOH$	− 0.61	[18]
$CO_2 + 2H^+ + 2e^- \rightarrow CO + H_2O$	− 0.53	[18]
$CO_2 + 4H^+ + 4e^- \rightarrow HCHO + H_2O$	− 0.48	[18]
$CO_2 + 6H^+ + 6e^- \rightarrow CH_3OH + H_2O$	− 0.38	[18]
$CO_2 + 8H^+ + 8e^- \rightarrow CH_4 + 2H_2O$	− 0.24	[18]
$2CO_2 + 8H^+ + 8e^- \rightarrow CH_3COOH + 2H_2O$	− 0.18	[19]
$2CO_2 + 12H^+ + 12e^- \rightarrow C_2H_4 + 4H_2O$	− 0.35	[19]
$2CO_2 + 12H^+ + 12e^- \rightarrow C_2H_5OH + 3H_2O$	− 0.33	[19]

[a]SHE standard hydrogen electrode

2.1 Nb doping

TiO_2, a nontoxic and inexpensive semiconductor photocatalyst, has a suitable electronic band structure for CO_2 reduction [28]. The electrons on the CB [$E_{CB} = − 0.50$ V (vs. SHE at pH 7)] are sufficiently energetic to reduce CO_2 into the majority of the products [29]. However, the adsorption and activation of CO_2 on TiO_2 are weak [30]. Nb element can act as the heteroatom dopant to replace Ti^{4+} and introduce structural defects such as Ti^{3+} into TiO_2 [31]. In addition to improving the charge separation efficiency of TiO_2, the structural defects and Nb atoms can also promote the adsorption and activation of CO_2 around the doped Nb atom. Qian et al. [23] used the electrochemical anodic oxidation method to substitute Ti^{4+} in TiO_2 with Nb^{5+} and obtain $Nb–TiO_2$ nanotube arrays. Nb^{5+} doping did not change the band gap of TiO_2 because the Nb^{5+} defect state was located above the bottom of the CB. Figure 2a shows that the amount of CO_2 adsorbed on $Nb–TiO_2$ was significantly higher than that on unmodified TiO_2. First-principle calculations suggested that CO_2 was adsorbed and activated on the $Nb–iO_2$ surface around the doped Nb atom. The X-ray photoelectron spectroscopy (XPS) C1s spectra in the dark showed that after CO_2 adsorption, $CO_2^{\delta-}$ species were formed on $Nb–TiO_2$ but not TiO_2 (Fig. 2b). It should be noted that $CO_2^{\delta-}$ represents the chemisorbed CO_2 species in a bent configuration that obtains electrons on $Nb–TiO_2$, which is different from the formation of linear CO_2^-. The increased number of active electrons on the surface of $Nb–TiO_2$ promoted the generation of $CO_2^{\delta-}$. $CO_2^{\delta-}$ could be transformed into HCOOH or CH_3O-, which could be further converted to CH_3CHO. Under the simulated solar light illumination at 200 mW cm^{-2} and using triethanolamine (TEOA) as the hole sacrificial agent, the CH_3CHO production rate on $Nb–TiO_2$ was up to 572 µmol·g^{-1}·h^{-1}, 2.86 times higher than that on TiO_2. The product selectivity toward CH_3CHO was

over 99% after 24 h. To date, CO and CH_4 are the primary products of photocatalytic CO_2 reduction by TiO_2 nanotube arrays, as reported in most works [32–35]. However, this study reported that $Nb–TiO_2$ nanotube arrays mainly reduce CO_2 to CH_3CHO. The authors proposed a possible mechanism for photocatalytic CO_2 reduction by the $Nb–TiO_2$ nanotube array with water as the reductant and TEOA as the sacrificial agent. When photogenerated holes reacted with TEOA to be consumed by producing $TEOA^+$, photogenerated electrons progressively reduced CO_2 to form $CO_2^{\delta-}$, formate, methoxy, and formyl species on the catalyst surface and finally generated CH_3CHO.

Unlike the above study, Truc et al. [36] reported that Nb^{5+} doping narrowed the band gap of TiO_2 due to the significant increase of Ti^{3+} in the $Nb–TiO_2$. Thus, compared with the pristine TiO_2, the generation rates of CH_4 and CO on $Nb–TiO_2$ increased to 268 and 109 µmol·g^{-1}·h^{-1} without any hole sacrificial agents under visible light illumination. Nogueira et al. [22] prepared Nb^{4+}-doped TiO_2 ($Nb^{4+}–TiO_2$) via the Pechini method and deposited Nb^0 on the surface of TiO_2 ($Nb^0–TiO_2$) via the sputtering deposition method. Under ultraviolet (UV) light (150 W mercury UV lamp) irradiation, the methanol yield on $Nb^{4+}–TiO_2$ was only 0.54–1.00 µmol·g^{-1}·h^{-1}, significantly lower than that on P25 consisting of 80% anatase and 20% rutile. Moreover, $Nb^0–TiO_2$ exhibited a lower methanol yield than $Nb^{4+}–TiO_2$. To sum up, the CO_2 reduction rates on Nb^{4+} and Nb^0-modified TiO_2 were significantly lower than that on $Nb^{5+}–TiO_2$, suggesting the photocatalytic activity of different valence states of Nb decreased in the following order: $Nb^{5+} > Nb^{4+} > Nb^0$.

High-entropy materials have attracted the attention for photocatalytic CO_2 reduction due to their high chemical stability and diverse electrical characteristics [37]. Li et al. [27] firstly synthesized Nb-containing high-entropy (Ti, Hf, Nb, Ta, Mo) nitride ceramic nanofibers (HENCNFs) via the electrospinning–calcination–nitridation method. HENCNFs exhibited strong adsorption of visible and near-infrared light. The production rates of CO and CH_4 were maintained at 469 and 242.5 µmol·g^{-1}·h^{-1}, respectively, after five 10 h cycles. A clear understanding of the photocatalytic mechanism of HENCNFs is a challenge, so the authors speculated that the combination of several metal elements in HENCNFs may contribute to hybridized cation orbitals, which promote the conversion of CO_2 to CO and CH_4.

2.2 Noble metal decoration

Nb-based perovskites are typical photocatalysts for CO_2 reduction due to their suitable electronic band structure [8], carrier separation property [38], and isolated redox sites [39]. Fresno et al. [40] reported that $NaNbO_3$ presented higher CO_2 conversion, electron efficiency, and CO
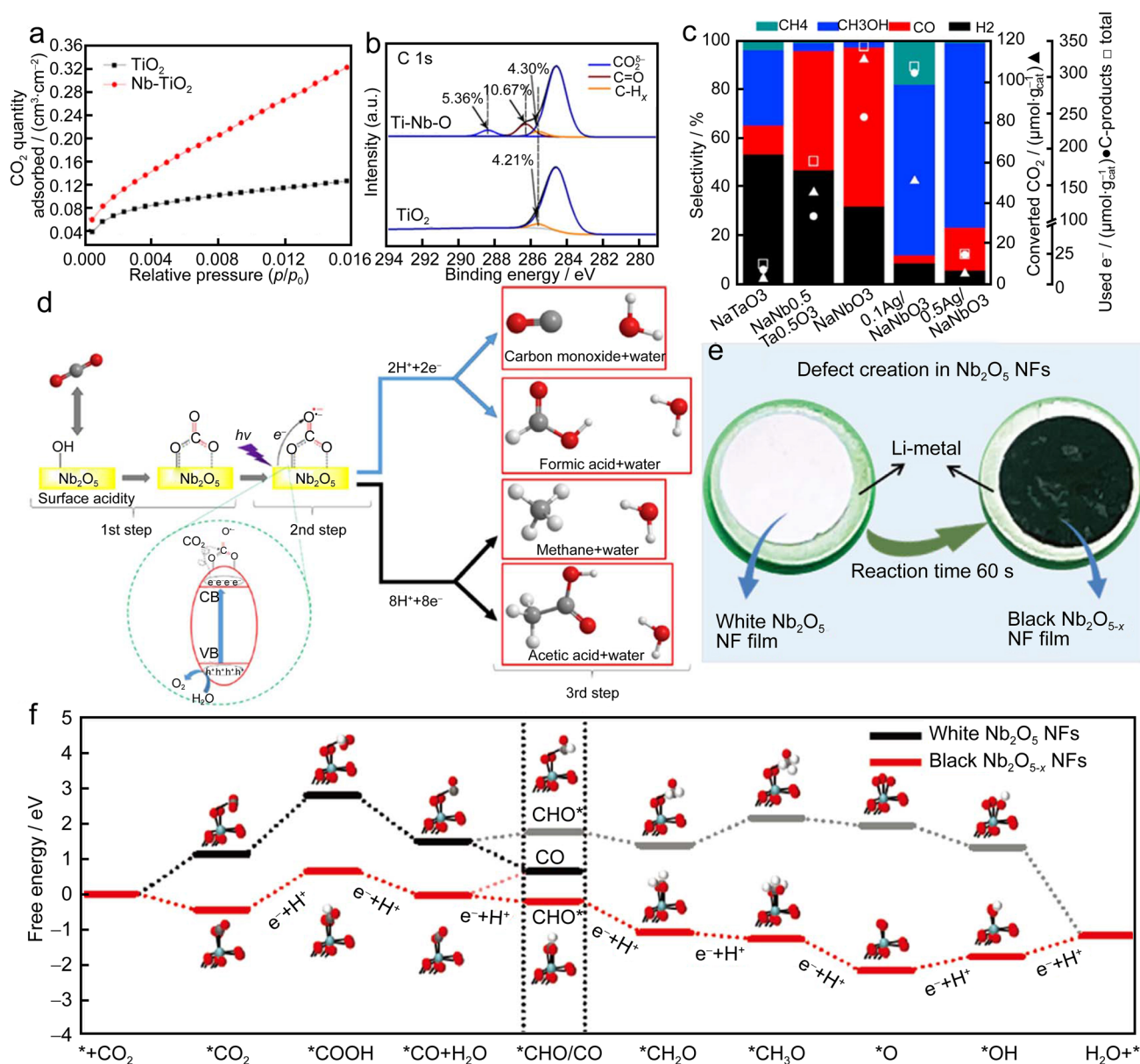
Fig. 2 **a** CO_2 quantities adsorbed on TiO_2 and Nb–TiO_2; **b** XPS C 1 s spectra of TiO_2 and Nb–TiO_2 after CO_2 adsorption in the dark. **a** and **b** are reproduced with permission from Ref. [23]. Copyright 2020 American Chemical Society. **c** Product selectivities (colored bars), CO_2 conversions (triangle symbols), and electron use (circle symbols: in C-products; open square symbols: in C-products + H_2) in photocatalytic reactions. Reproduced with permission from Ref. [40]. Copy-

right 2021 Elsevier. **d** Proposed pathways for CO_2 photoreduction adsorbed on the acid surface of Nb_2O_5 (*hv*: photon energy). Reproduced with permission from Ref. [44]. Copyright 2019 Elsevier. **e** A sketch to show the room-temperature defect control strategy; **f** calculated Gibbs free energy diagram for CO_2 reduction toward CO and CH_4 over the white Nb_2O_5 and black Nb_2O_{5-x} NFs. **e** and **f** are reproduced with permission from Ref. [46]. Copyright 2022 Wiley–VCH

selectivity (Fig. 2c) than $NaTaO_3$ and $NaNb_{0.5}Ta_{0.5}O_3$. In $NaNbO_3$, Nb^{5+} was the main active site, and Nb^{4+} was not conducive to CO_2 reduction. However, bare $NaNbO_3$ produced plenty of H_2, competing with CO_2 reduction to consume photogenerated electrons. Noble metal (e.g., Ag, Au, and Pt) decoration strongly influences the selectivity of CO_2 reduction products due to their differences in the adsorption/activation of reactant molecules [41]. Noble

metals with a high ability to extract photogenerated electrons from base photocatalysts can enhance the surface photogenerated electron density, promoting profound CO_2 reduction. Thus, they loaded Ag nanoparticles to $NaNbO_3$ (Ag/$NaNbO_3$). Under UV illumination, CO_2 tended to be adsorbed and activated on Ag-related sites. The reduction product, CO, could be strongly adsorbed on Ag^+ sites on the Ag/$NaNbO_3$ surface. The Ag decoration also promoted

the transfer of photogenerated electrons to CO_2 and reduction intermediates. More electrons are required to convert CO_2 to methanol than CO. The enhanced CO adsorption and electron transfer on $Ag/NaNbO_3$ surface were beneficial for the further conversion of CO to methanol (Fig. 2c), which consumes a large number of protons to inhibit H_2 formation.

2.3 Surface acidity adjustment

The surface acid–base property of photocatalysts significantly affected CO_2 reduction performance [42]. Bhattacharyya et al. [11] proposed that the surface acid sites as electron acceptors provided favorable situations for the formation of bidentate carbonates during CO_2 reduction. Nb_2O_5, as a semiconductor with a highly acidic surface, was previously reported to show photocatalytic activity for pollution degradation [43]. da Silva et al. [44] firstly applied Nb_2O_5 to photocatalytic CO_2 reduction and found that niobic acid ($Nb_2O_5 \cdot nH_2O$) was the active phase. The reaction rate and selectivity of CO_2 reduction were significantly correlated with the surface acidity of Nb_2O_5. High surface acidity of Nb_2O_5 tended to promote the conversion of CO_2 into CO, HCOOH, and CH_3COOH, while low surface acidity would favor the conversion of CO_2 into CH_4. The photocatalytic CO_2 reduction paths on Nb_2O_5 are shown in Fig. 2d. The acid sites on Nb_2O_5 (surface −OH) drive the CO_2 adsorption and activation through the bidentate coordination of the CO_2 molecule.

2.4 Oxygen vacancy engineering

Nb_2O_5 has a wide band gap (∼ 3.0 eV) [45] and is less capable of converting CO_2 into CH_4. Lin et al. [46] prepared flexible mesoporous black Nb_2O_{5-x} nanofibers (NFs) for visible light–driven CO_2 reduction to CH_4 by electrospinning and diffusion–reduction methods at room temperature (Fig. 2e). The abundant oxygen vacancies and unsaturated Nb in black Nb_2O_{5-x} NFs lowered the band gap to 2.25 eV and broadened the absorption edge of Nb_2O_5 from UV to visible light range. The mesoporous structure formed from polyvinyl pyrrolidone could provide more active sites for CO_2 reduction. By inhibiting CO desorption and turning the conversion from CO* to *CHO (* represents catalyst surface) into a spontaneous thermogenic process, the oxygen vacancies and unsaturated Nb active dual sites significantly boosted CO_2 adsorption and activation as well as increased the CH_4 selectivity (Fig. 2f). The CH_4 selectivity on black Nb_2O_{5-x} NFs reached 64.8%, while it was 0% on white Nb_2O_5 NFs. Moreover, dual

active sites promoted photogenerated carrier separation as carrier capture centers.

2.5 Heterojunction construction

The rate of photocatalytic CO_2 reduction was dependent on the photogenerated electron yield and transfer [47]. Jiang et al. [48] constructed a two-dimensional (2D) heterojunction between $KCa_2Nb_3O_{10}$ nanosheets and $ZnIn_2S_4$ nanosheets ($ZnIn_2S_4/KCNO$), which efficiently promoted charge separation and transfer (Fig. 3a). In composite materials, the ultrathin structure of $KCa_2Nb_3O_{10}$ perovskite was beneficial for the rapid transmission of photogenerated electrons. The nanoflower structure of $ZnIn_2S_4$ exposed more active sites for reactants and enhanced the production and transmission of protons from water oxidation (Fig. 3b). The CO production rate of composite material was 4.69 $\mu mol \cdot g^{-1} \cdot h^{-1}$, up to 1.95 and 12.31 times that of pure $KCa_2Nb_3O_{10}$ nanosheets and $ZnIn_2S_4$ nanosheets, respectively.

Due to its limited reduction capacity, photogenerated electrons on the CB of Nb–TiO_2 cannot reduce CO_2 to produce HCOOH. Although the reduction ability of photogenerated electrons on the CB of g-C_3N_4 was sufficient to convert CO_2 into HCOOH, the separation efficiency of electron/hole pairs by g-C_3N_4 is low [49]. The heterojunction construction can significantly promote charge separation and maintain good adsorption capacity of g-C_3N_4 to CO_2. Thus, Truc et al. [36] constructed the direct Z-scheme heterojunction between Nb–TiO_2 and g-C_3N_4 (Nb–TiO_2/g-C_3N_4). The Z-scheme heterojunction not only facilitated charge separation to boost CH_4 and CO generation, but also led to the formation of HCOOH due to the strong reduction ability of the photogenerated electrons on the CB of g-C_3N_4 (Fig. 3c).

3 Electrocatalytic CO_2 reduction

During CO_2 reduction, the next step after CO_2 adsorption is the activation of the CO_2 molecule. Two possible activation pathways of CO_2 on the catalyst surface during the electrocatalytic reduction [50] are as shown in Eqs. (1) and (2):

$$* + CO_2 + H^+ + e^- \rightarrow {}^*COOH \tag{1}$$

$$* + CO_2 + H^+ + e^- \rightarrow {}^*OCHO \tag{2}$$

Equations (1) and (2) are the electron-coupled proton transfer reactions, which determine the product selectivity [51]. *COOH is more likely to be the intermediate for CO generation, while *OCHO is more feasible to evolve into HCOOH [52]. The products of CO_2 activation depend on the composition and structure of catalysts [51]. Through density
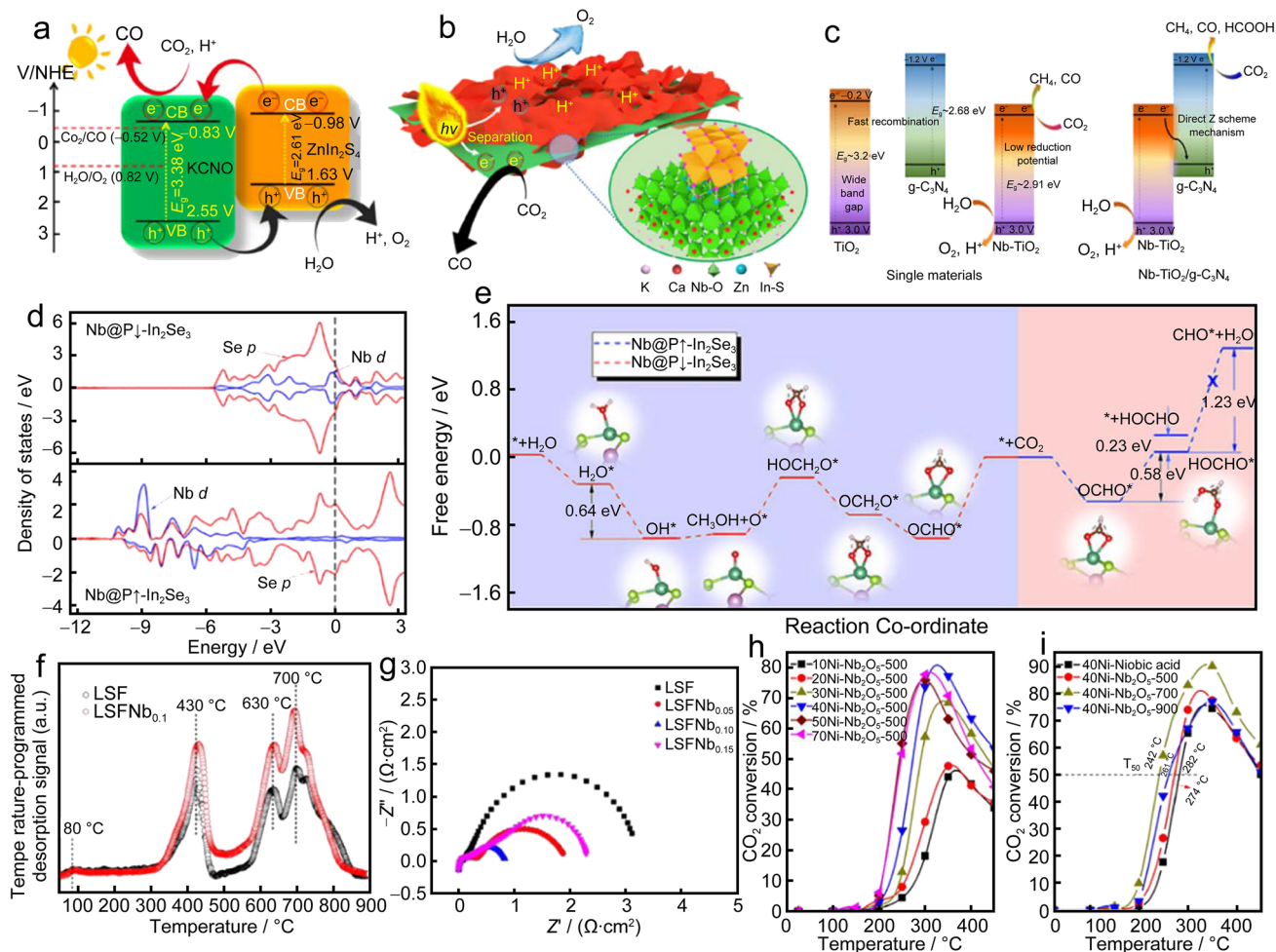
Fig. 3 **a** Charge separation and transfer in $ZnIn_2S_4$/KCNO heterojunction (NHE: normal hydrogen electrode). **b** Possible photocatalytic CO_2 reduction mechanism over $ZnIn_2S_4$/KCNO 2D/2D nanosheet heterojunction photocatalysts. **a** and **b** are reproduced with permission from Ref. [48]. Copyright 2021 Elsevier. **c** Direct Z-scheme mechanism of Nb–TiO_2/g-C_3N_4 for the reduction of CO_2. Reproduced with permission from Ref. [36]. Copyright 2019 Elsevier. **d** Partial density of states of Nb@P↓-In_2Se_3 and Nb@P↑-In_2Se_3; **e** calculated paths for CO_2 reduction on Nb@In_2Se_3. **d** and **e** are reproduced with permission from Ref. [55], licensed under CC BY 4.0. **f** Temperature-programmed desorption of CO_2 on LSF and LSFNb$_{0.1}$; **g** the EIS of the three-electrode half cells measured in pure CO_2 atmosphere at applied voltages of 0.8 V. **f** and **g** are reproduced with permission from Ref. [57]. Copyright 2021 Elsevier. **h** CO_2 conversion for Ni-loading Nb_2O_5 with different Ni loading and **i** 40Ni–Nb_2O_5 with the pre-calcination temperatures of 500, 700, and 900 ℃. **h** and **i** are reproduced with permission from Ref. [69]. Copyright 2019 Elsevier

functional theory (DFT) calculations, Zhao et al. [53] analyzed 190 transition metal near-surface alloys (NSAs), promising catalysts for electrocatalytic CO_2 reduction. Among 20 NSAs that could selectively reduce CO_2 to HCOOH, Pd/W, Au/Hf, and Au/Zr were predicted to be the most active catalysts with a lower overpotential. On Au- and Ag-containing NSAs, *COOH may be formed during the initial hydrogenation step of CO_2. Considering the weaker adsorption of *CO and stronger adsorption of *COOH, Ag/Hf and Ag/Zr were the most active catalysts with the higher overpotential. They discovered that the higher difference in electronegativity between metal pairs in NSA catalysts was advantageous for the selective electrocatalytic reduction of CO_2 to CO.

Due to the ability to form CO and the strong adsorption of CO, Ag/Ta and Ag/Nb were suitable candidates for electrocatalytic CO_2 reduction to CH_3OH and C_2H_4. Theoretical calculation researches suggest that Nb on PdH(111) could effectively reduce the formation energy of *COOH, maintain moderate CO adsorption energy, and inhibit the conversion of *COOH to *H [54]. Because of these advantages, Nb on PdH(111) exhibited better kinetic activities to generate more CO selectively. Ju et al. [55] proposed that single atom Nb on ferroelectric In_2Se_3 (Nb@In_2Se_3) was an effective catalyst for electrocatalytic CO_2 reduction based on comprehensive DFT computations. Figure 3d shows that the polarization direction of In_2Se_3 determined the final products (CH_3OH

and HCOOH) on Nb@In_2Se_3 due to the great difference of the d band center between Nb@In_2Se_3 with the opposite polarization directions (Nb@P↓-In_2Se_3 and Nb@P↑-In_2Se_3). Figure 3e depicts the possible pathway of CO_2 reduction on Nb@In_2Se_3. However, in molecular electrocatalysis, Guo et al. [56] found that the product of the electrocatalytic CO_2 reduction by Nb/corrole complex was CH_4. The potential determining step was the CH_2O^* hydrogenation to CH_2OH^*. The above theoretical calculation results show that the supports in Nb-based catalysts are critical to the process and products of electrocatalytic CO_2 reduction.

3.1 Nb doping

In most studies on electrocatalytic CO_2 reduction by Nb-containing catalysts, CO was the main product [12, 15, 57]. Abbasi et al. [15] doped Nb into the crystal lattice of MoS_2 without changing its lattice parameters for the effective electrocatalytic reduction of CO_2 to CO. Nb doping enhanced the catalytic activity of active sites and increased active sites by 50% through activating edge Mo atoms due to the fewer valence states of Nb than those of Mo. The strong adsorption of $^*CO$ on MoS_2 was weakened by Nb doping, which simultaneously kept the exergonic formation of $^*COOH$. The CO formation turnover frequency of Nb–MoS_2 was one order of magnitude higher than that of MoS_2, and the CO selectivity was 82%, with the potential of − 0.8 V (vs. SHE at pH 7).

The solid oxide electrolysis cell is an effective electrocatalytic technique for CO_2 reduction by utilizing industrial waste heat [58]. Perovskites are promising fuel electrode materials for direct CO_2 electrolysis due to their mixed ionic–electronic conductivity [59] and redox stability [60]. Wang et al. [57] prepared Nb-doping ferrite-based perovskite oxides, $La_{0.6}Sr_{0.4}Fe_{1−x}Nb_xO_{3-\delta}$. Figure 3f reveals the stronger chemical adsorption of CO_2 on $La_{0.6}Sr_{0.4}Fe_{0.9}Nb_{0.1}O_{3-\delta}$ ($LSFNb_{0.1}$) than on $La_{0.6}Sr_{0.4}FeO_{3-\delta}$ (LSF). The substitution of Fe by Nb increased the surface oxygen vacancies to promote CO_2 adsorption and carbonate dissociation. Figure 3g shows that $La_{0.6}Sr_{0.4}Fe_{1−x}Nb_xO_{3-\delta}$ exhibited a much lower polarization resistance (the distance between the intercept of high-frequency and low-frequency electrochemical impedance spectrum (EIS) on the real axis) than LSF. This result suggested that Nb doping improved the electrode reaction kinetics in favor of electron transfer to CO_2. Nb doping prevented the Sr segregation in $La_{0.6}Sr_{0.4}Fe_{1−x}Nb_xO_{3-\delta}$ during high-temperature CO_2 electrolysis, and the material displayed remarkable redox stability.

3.2 Noble metal decoration

Au and Ag are the most studied noble metals for electrocatalytic CO_2 reduction to CO due to their weak adsorption of CO [61]. Current research on Au- and Ag-based
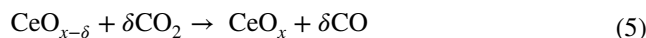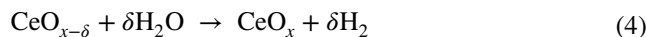
electrocatalysts has focused on increasing the faradaic efficiency of CO production rather than achieving the appropriate CO/H_2 ratio between 0.5 and 2 [62], which is essential for subsequent utilization. Thus, Nian et al. [63] selected NbC and NbN with high mechanical stability and electric conductivity as supports to tune the active Ag and Au species for the controllable CO/H_2 ratio. NbC and NbN transferred electrons to Au and Ag to optimize their electronic structure, thereby lowering the free energy of the potential determining step and the formation of $^*COOH$. Therefore, the CO production rate and selectivity on Ag and Au supported on NbC and NbN were enhanced, resulting in a CO/H_2 ratio between 0.5 and 2.

4 Thermocatalytic CO_2 reduction

Thermocatalytic CO_2 reduction exhibits a higher reaction rate and product yield than photocatalysis and electrocatalysis, and the products do not require separation [64, 65]. As the typical thermocatalytic CO_2 reduction process, the reduction reaction from CO_2 to CO by H_2 is endothermic ($CO_2 + H_2 → CO + H_2O$, $\Delta H = 41.2$ kJ·$mol^{−1}$, $T = 298.15$ K) [66]. So the temperature rise is conducive to the reaction. Nb-containing thermocatalysts currently used for CO_2 reduction include Nb-doping CeO_2 [67, 68], Nb_2O_5 [24, 69], Nb-particle-decorated [70, 71] and Nb_2O_5 particle-decorated catalysts [24].

4.1 Nb doping

Due to the ease of forming surface oxygen vacancies and Ce^{3+}/Ce^{4+} redox couple, CeO_2 is widely used in a variety of thermocatalytic applications [72]. The thermocatalytic CO_2 reduction cycle over Ce-based catalysts is as shown in Eqs. (3)–(5):

$$CeO_x → CeO_{x−\delta} + \delta/2O_2 \qquad (3)$$

$$CeO_{x−\delta} + \delta H_2O → CeO_x + \delta H_2 \qquad (4)$$

$$CeO_{x−\delta} + \delta CO_2 → CeO_x + \delta CO \qquad (5)$$

In the above redox cycle, x is lower than 2; δ is the oxygen exchange capacity (OEC), which is a crucial parameter of material optimization because it is directly proportional to the product amount generated in a single cycle per unit mass catalyst [73]. Tetravalent metal doping is a potential modification strategy for increasing OEC and maintaining thermo-mechanical stability simultaneously because the hetero-metal atoms could enhance the redox activity of $CeO_{x−\delta}$ without changing the oxygen nonstoichiometry [74, 75]. Jacot et al. [67] found that Zr(IV)-, Hf(IV)-, Ta(IV)-, and

Nb(IV)-doped CeO_2 had a higher OEC than pure CeO_2 and maintained high thermo-mechanical stability after evaluating 26 metals that could adopt an oxidation state of +IV. They hypothesized that the effective dopant radius was closely related to the OEC and that the optimal radius for the maximal OEC was around 0.08 nm. In their subsequent work, they found that Hf, Zr, and Nb doping exhibited long-term stability during the 50 redox cycles of CO_2 reduction. The homogeneous dispersion of dopants in CeO_2 was a crucial stability condition [76]. Muhich et al. [68] proposed that using trivalent and pentavalent cations, paired charge-compensating doped ceria can boost the flexibility of CO_2 and H_2O conversion on CeO_2 more flexibly while maintaining its thermo-mechanical stability. M(III)/Nb(V) (M = La, Y, and Sc) co doping enhanced the reduction ability, and the lower oxidation state of the trivalent dopant could result in a lower oxygen vacancy formation energy.

4.2 Nb_2O_5

Based on the activation of CO_2 on Nb_2O_5 and the strong metal support interaction (SMSI) for metals supported on Nb_2O_5, Gnanakumar et al. [69] loaded Ni on Nb_2O_5 for the catalytic hydrogenation of CO_2 to CH_4. All Ni-loading Nb_2O_5 catalysts showed the highest conversion of CO_2 methanation at the reaction temperatures below 350 ℃ (Fig. 3h), hence inhibiting CO formation. Ni aggregation, the production of volatile $Ni(CO)_4$, and coke deposition have the potential to inhibit catalytic activity. By pre-calcining Nb_2O_5, they modified the surface acid sites to enhance the interaction between Ni and Nb_2O_5. The enhancement of the SMSI effect and strong acid sites increased the CO_2 conversion to almost 90% and reduced the T_{50} (the temperature at which 50% conversion had occurred) to 242 ℃ (Fig. 3i).

4.3 Nb or Nb_2O_5 particle decoration

Santana et al. [24] doped Cu/ZnO with Nb_2O_5 as a promoter for CO_2 reduction to CH_3OH in light of the fact that a small amount of Nb_2O_5 could enhance the CO_2 reduction activity and the structural stability of the catalyst. Compared with Cu/ZnO (UN), the loading of Nb_2O_5 increased the dispersion and metallic area of Cu. Among the four synthesis methods of Cu/ZnO/Nb_2O_5 (i.e., coprecipitation (CP), deposition−precipitation (DP), wet impregnation (WI), and incipient wetness impregnation (IW)), the CP method resulted in the largest specific surface area (48 $m^2·g^{-1}$), the highest Cu dispersion (Fig. 4a) and metallic area (15.6 $m^2·g^{-1}$), and the greatest CO_2 absorption. Thus, Cu/ZnO/Nb_2O_5-CP

exhibited the highest CH_3OH space − time yield (STY) of 70.1 $g·kg^{-1}·h^{-1}$ at 200 ℃ (Fig. 4b). The CH_3OH selectivity of Cu/ZnO/Nb_2O_5-CP was 70.2%, 1.9 times higher than that of Cu/ZnO (Fig. 4c). Noh et al. [70] also proved that the co-loading of Nb and Cu on SiO_2 significantly increased the CO_2 conversion and CH_3OH selectivity. The high CH_3OH selectivity resulted from abundant Lewis acid Nb sites, which enhanced the stabilization of intermediates (formate and methoxy) during the CO_2 reduction to CH_3OH.

5 Conclusion and future perspectives

This minireview summarizes various Nb-containing catalysts, such as Nb_2O_5, Nb-based perovskites, Nb-doping catalysts (e.g., Nd–TiO_2, Nd–MoS_2, and Nd–CeO_2), and Nb particle-decorated catalysts (e.g., Nb@In_2Se_3 and Cu/Nb@SiO_2), for the application of photo-, electro-, and thermocatalytic reduction of CO_2. In Nb_2O_5 catalysts, $Nb_2O_5·nH_2O$ is the active species, Nb^{5+} is the main active site, and the adjustment of acid sites can change the product selectivity. Nb doping can not only enhance the thermo-mechanical and redox stability but also optimize the electron structure of the base catalysts to increase the number of active sites and enhance the activity of the active site. Moreover, the base catalysts affected the product selectivity and potential determining step on Nb doping and Nb-loaded catalysts.

The prospects for the design and optimization of Nb-containing catalysts in CO_2 reduction are as follows:

i. Theoretical calculations have ruled out many active Nb-containing catalysts, but only a few have been confirmed experimentally. Thus, it is essential to synthesize these Nb-containing catalysts with prospective catalytic activity and investigate the mechanism of the CO_2 reduction reaction.

ii. There are few reports on Nb-based metal–organic framework catalysts for catalytic CO_2 reduction. Metal–organic framework catalysts have an enormous specific surface area and abundant pores in favor of CO_2 adsorption. In addition, Nb in metal–organic frameworks can be highly exposed and designed to be coordinately unsaturated, which is expected to promote CO_2 activation.

iii. To improve the catalytic efficiency of CO_2 reduction without any sacrificial agents, Nb-containing catalysts can be designed and applied to photoelectrocatalysis CO_2 reduction. The photoelectrocatalytic CO_2 reduction can reduce energy consumption, enhance carrier separation, and realize the quick transfer of multi electrons and protons in favor of forming desired long-chain organics.
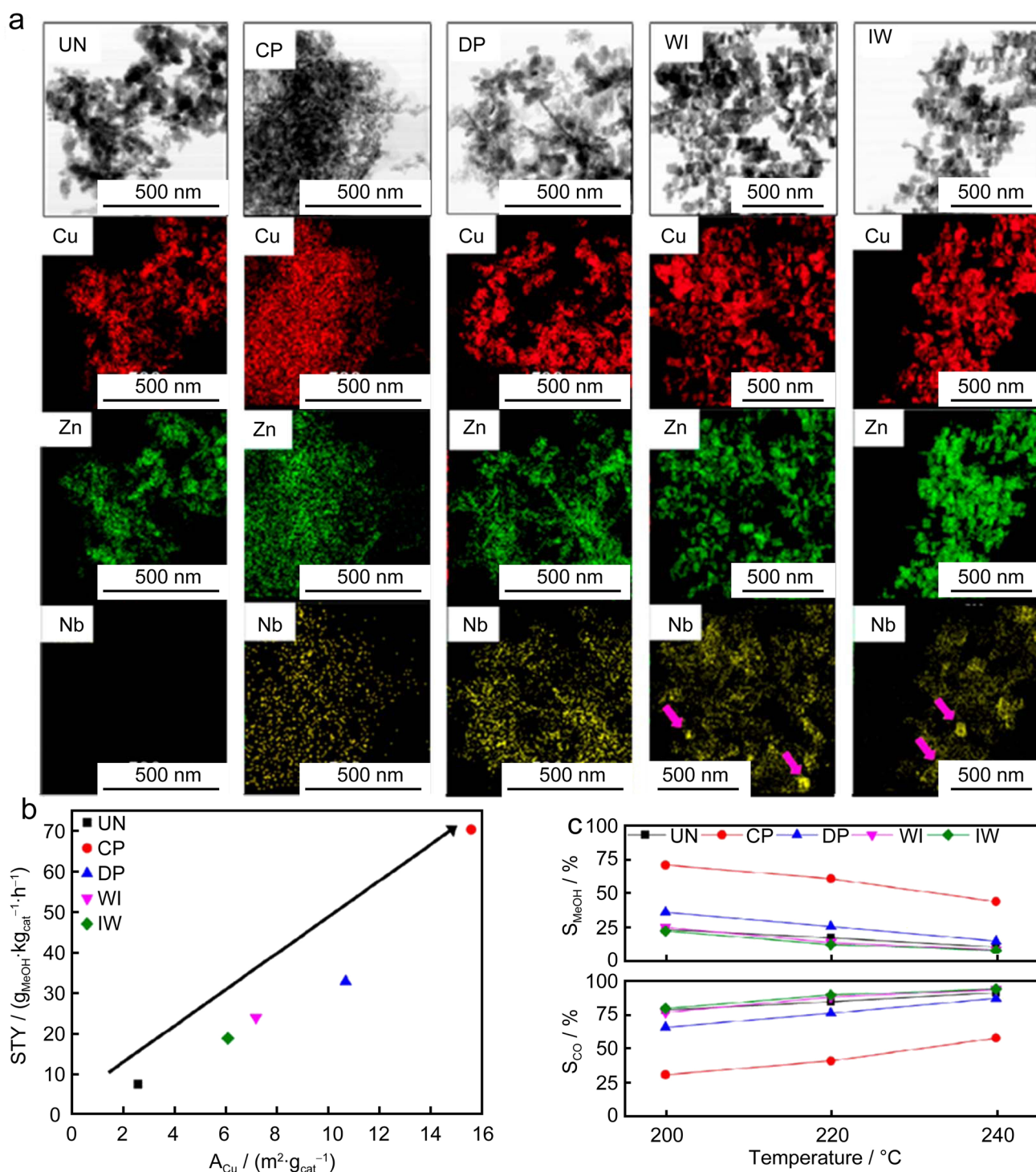
Fig. 4 a Transmission electron microscope–energy dispersive spectroscopy elemental mappings of Cu/ZnO, Cu/ZnO/Nb$_2$O$_5$-CP, Cu/ZnO/Nb$_2$O$_5$-DP, Cu/ZnO/Nb$_2$O$_5$-WI, and Cu/ZnO/Nb$_2$O$_5$-IW; **b** the STY of CH$_3$OH at 200 ℃; **c** the CH$_3$OH (S_{MeOH}) and CO (S_{CO}) selectivity (reaction conditions: H$_2$/CO$_2$ = 3, gaseous hourly space velocity = 6 L·g^{-1}·h^{-1}, and 3 MPa). Reproduced with permission from Ref. [24]. Copyright 2021 American Chemical Society

Declarations

Conflict of interest The authors declare no conflict of interest.

References

1. Qiao JL, Liu YY, Hong F, Zhang JJ. A review of catalysts for the electroreduction of carbon dioxide to produce low-carbon fuels. Chem Soc Rev. 2014;43:631.

2. Patil SB, Wang DY. Electrochemical reactions towards the formation of heteroatomic bonds beyond CO_2 and N_2 reduction. Sustain Energy Fuels. 2022;6:3283.

3. Zhu DD, Liu JL, Qiao SZ. Recent advances in inorganic heterogeneous electrocatalysts for reduction of carbon dioxide. Adv Mater. 2016;28:3423.

4. Ye WX, Guo XL, Ma TL. A review on electrochemical synthesized copper-based catalysts for electrochemical reduction of CO_2 to C_{2+} products. Chem Eng J. 2021;414: 128825.

5. White JL, Baruch MF, Pander JE, Hu Y, Fortmeyer IC, Park JE, Zhang T, Liao K, Gu J, Yan Y, Shaw TW, Abelev E, Bocarsly AB. Light-driven heterogeneous reduction of carbon dioxide: photocatalysts and photoelectrodes. Chem Rev. 2015;115:12888.

6. Tackett BM, Gomez E, Chen JGG. Net reduction of CO_2 via its thermocatalytic and electrocatalytic transformation reactions in standard and hybrid processes. Nat Catal. 2019;2:381.

7. Birdja YY, Perez-Gallent E, Figueiredo MC, Gottle AJ, Calle-Vallejo F, Koper MTM. Advances and challenges in understanding the electrocatalytic conversion of carbon dioxide to fuels. Nat Energy. 2019;4:732.

8. Nunes BN, Lopes OF, Patrocinio AOT, Bahnemann DW. Recent advances in niobium-based materials for photocatalytic solar fuel production. Catalysts. 2020;10:126.

9. Kang SM, Miao RR, Guo JF, Fu JX. Sustainable production of fuels and chemicals from biomass over niobium based catalysts: a review. Catal Today. 2021;374:61.

10. Romo JE, Bollar NV, Zimmermann CJ, Wettstein SG. Conversion of sugars and biomass to furans using heterogeneous catalysts in biphasic solvent systems. ChemCatChem. 2018;10:4819.

11. Bhattacharyya K, Danon A, Vijayan BK, Gray KA, Stair PC, Weitz E. Role of the surface Lewis acid and base sites in the adsorption of CO_2 on titania nanotubes and platinized titania nanotubes: an in situ FT-IR study. J Phys Chem C. 2013;117:12661.

12. Zhang J, Xie K, Wei HS, Qin QQ, Qi WT, Yang LM, Ruan C, Wu YC. In situ formation of oxygen vacancy in perovskite $Sr_{0.95}Ti_{0.8}Nb_{0.1}M_{0.1}O_3$ (M = Mn, Cr) toward efficient carbon dioxide electrolysis. Sci Rep. 2014;4:7082.

13. Lopez M, Broderick L, Carey JJ, Vines F, Nolan M, Illas F. Tuning transition metal carbide activity by surface metal alloying: a case study on CO_2 capture and activation. Phys Chem Chem Phys. 2018;20:22179.

14. Din IU, Shaharun MS, Subbarao D, Naeem A, Hussain F. Influence of niobium on carbon nanofibres based Cu/ZrO_2 catalysts for liquid phase hydrogenation of CO_2 to methanol. Catal Today. 2016;259:303.

15. Abbasi P, Asadi M, Liu C, Sharifi-Asl S, Sayahpour B, Behranginia A, Zapol P, Shahbazian-Yassar R, Curtiss LA, Salehi-Khojin A. Tailoring the edge structure of molybdenum disulfide toward electrocatalytic reduction of carbon dioxide. ACS Nano. 2017;11:453.

16. Wu XC, Lang JY, Sun ZX, Jin FM, Hu YH. Photocatalytic conversion of carbon monoxide: from pollutant removal to fuel production. Appl Catal B. 2021;295:120312.

17. Huang XY, Gu WY, Ma YF, Liu D, Ding NK, Zhou L, Lei JY, Wang LZ, Zhang JL. Recent advances of doped graphite carbon nitride for photocatalytic reduction of CO_2: a review. ResChem Intermediat. 2020;46:5133.

18. Lu S, Lou FL, Yu ZX. Recent progress in two-dimensional materials for electrocatalytic CO_2 reduction. Catalysts. 2022;12:228.

19. Kunene T, Xiong L, Rosenthal J. Solar-powered synthesis of hydrocarbons from carbon dioxide and water. P Natl Acad Sci USA. 2019;116:9693.

20. Habisreutinger SN, Schmidt-Mende L, Stolarczyk JK. Photocatalytic reduction of CO_2 on TiO_2 and other semiconductors. Angew Chem Int Edit. 2013;52:7372.

21. Corma A, Garcia H. Photocatalytic reduction of CO_2 for fuel production: possibilities and challenges. J Catal. 2013;308:168.

22. Nogueira MV, Lustosa GMMM, Kobayakawa Y, Kogler W, Ruiz M, Monteiro ES, Zaghete MA, Perazolli LA. Nb-doped TiO_2 photocatalysts used to reduction of CO_2 to methanol. Adv Mater Sci Eng. 2018;2018:7326240.

23. Qian XZ, Yang WY, Gao S, Xiao J, Basu S, Yoshimura A, Shi YF, Meunier V, Li Q. Highly selective, defect-induced photocatalytic CO_2 reduction to acetaldehyde by the Nb-doped TiO_2 nanotube array under simulated solar illumination. ACS Appl Mater Interfaces. 2020;12:55982.

24. Santana CS, Shine LS, Vieira LH, Passini RJ, Urquieta-Gonzalez EA, Assaf EM, Gomes JF, Assaf JM. Effect of the synthesis method on physicochemical properties and performance of Cu/ZnO/Nb_2O_5 catalysts for CO_2 hydrogenation to methanol. Ind Eng Chem Res. 2021;60:18750.

25. Marszewski M, Cao SW, Yu JG, Jaroniec M. Semiconductor-based photocatalytic CO_2 conversion. Mater Horizons. 2015;2:261.

26. Shi HF, Wang TZ, Chen J, Zhu C, Ye JH, Zou ZG. Photoreduction of carbon dioxide over $NaNbO_3$ nanostructured photocatalysts. Catal Lett. 2011;141:525.

27. Li W, Sun YA, Ye L, Han WJ, Chen FH, Zhang JL, Zhao T. Preparation of high entropy nitride ceramic nanofibers from liquid precursor for CO_2 photocatalytic reduction. J Am Ceram Soc. 2022;105:3729.

28. Tahir M, Amin NS. Photocatalytic reduction of carbon dioxide with water vapors over montmorillonite modified TiO_2 nanocomposites. Appl Catal B. 2013;142:512.

29. Devaraji P, Gopinath CS. Pt - g-C_3N_4-(Au/TiO_2): Electronically integrated nanocomposite for solar hydrogen generation. Int J Hydrog Energy. 2018;43:601.

30. Chang XX, Wang T, Gong JL. CO_2 photo-reduction: insights into CO_2 activation and reaction on surfaces of photocatalysts. Energy Environ Sci. 2016;9:2177.

31. Kitahara M, Shimasaki Y, Matsuno T, Kuroda Y, Shimojima A, Wada H, Kuroda K. The critical effect of niobium doping on the formation of mesostructured TiO_2: Single-crystalline ordered mesoporous Nb–TiO_2 and plate-like Nb–TiO_2 with ordered mesoscale dimples. Chem Eur J. 2015;21:13073.

32. Ikreedeegh RR, Tahir M. Photocatalytic CO_2 reduction to CO and CH_4 using g-C_3N_4/RGO on titania nanotube arrays (TNTAs). J Mater Sci. 2021;56:18989.

33. Kar P, Farsinezhad S, Mahdi N, Zhang Y, Obuekwe U, Sharma H, Shen J, Semagina N, Shankar K. Enhanced CH_4 yield by photocatalytic CO_2 reduction using TiO_2 nanotube arrays grafted with Au, Ru, and ZnPd nanoparticles. Nano Res. 2016;9:3478.

34. Low JX, Qiu SQ, Xu DF, Jiang CJ, Cheng B. Direct evidence and enhancement of surface plasmon resonance effect on Ag-loaded TiO_2 nanotube arrays for photocatalytic CO_2 reduction. Appl Surf Sci. 2018;434:423.

35. Zubair M, Kim H, Razzaq A, Grimes CA, In SI. Solar spectrum photocatalytic conversion of CO_2 to CH_4 utilizing TiO_2 nanotube arrays embedded with graphene quantum dots. J CO2 Util. 2018;26:70.

36. Truc NTT, Bach LG, Hanh NT, Pham TD, Chi NTPC, Tran DT, Nguyen MV, Nguyen VN. The superior photocatalytic activity of Nb doped TiO_2/g–C_3N_4 direct Z-scheme system for efficient conversion of CO_2 into valuable fuels. J Colloid Interface Sci. 2019;540:1.

37. Akrami S, Murakami Y, Watanabe M, Ishihara T, Arita M, Fuji M, Edalati K. Defective high-entropy oxide photocatalyst with high activity for CO_2 conversion. Appl Catal B. 2022;303:120896.

38. Portugal GR, Barbosa GG, Arantes JT. $NaNbO_3$/$NaTaO_3$ superlattices: Cation-ordering improved band-edge alignment for water splitting and CO_2 photocatalysis. Langmuir. 2021;37:4493.

39. Hernandez-Alonso MD, Fresno F, Suarez S, Coronado JM. Development of alternative photocatalysts to TiO_2: challenges and opportunities. Energy Environ Sci. 2009;2:1231.

40. Fresno F, Galdon S, Barawi M, Alfonso-Gonzalez E, Escudero C, Perez-Dieste V, Huck-Iriart C, O'Shea VAD. Selectivity in UV photocatalytic CO_2 conversion over bare and silver-decorated niobium-tantalum perovskites. Catal Today. 2021;361:85.

41. Fu JW, Jiang KX, Qiu XQ, Yu JG, Liu M. Product selectivity of photocatalytic CO_2 reduction reactions. Mater Today. 2020;32:222.

42. Pu Y, Luo YD, Wei XQ, Sun JF, Li LL, Zou WX, Dong L. Synergistic effects of Cu_2O-decorated CeO_2 on photocatalytic CO_2 reduction: Surface Lewis acid/base and oxygen defect. Appl Catal B. 2019;254:580.

43. Lopes OF, Paris EC, Ribeiro C. Synthesis of Nb_2O_5 nanoparticles through the oxidant peroxide method applied to organic pollutant photodegradation: a mechanistic study. Appl Catal B. 2014;144:800.

44. da Silva GTST, Nogueira AE, Oliveira JA, Torres JA, Lopes OF, Ribeiro C. Acidic surface niobium pentoxide is catalytic active for CO_2 photoreduction. Appl Catal B. 2019;242:349.

45. Shao RY, Zeng X, Cao ZZ, Dong HJ, Wang LY, Wang F, Liu JR, Li Z, Liang QH. A novel Ag_3PO_4/Nb_2O_5 fiber composite with enhanced photocatalytic performance and stability. Rsc Adv. 2015;5: 102101.

46. Lin X, Xia SH, Zhang L, Zhang YY, Sun SM, Chen YH, Chen S, Ding B, Yu JY, Yan JH. Fabrication of flexible mesoporous black Nb_2O_5 nanofiber films for visible-light-driven photocatalytic CO_2 reduction into CH_4. Adv Mater. 2022;34:2200756.

47. Ran JR, Jaroniec M, Qiao SZ. Cocatalysts in semiconductor-based photocatalytic CO_2 reduction: achievements, challenges, and opportunities. Adv Mater. 2018;30:1704649.

48. Jiang DL, Zhang QX, Chen DH, Wen BW, Song Q, Zhou CJ, Li D. $KCa_2Nb_3O_{10}$/$ZnIn_2S_4$ nanosheet heterojunctions with improved charge separation efficiency for efficient photocatalytic CO_2 reduction. J Alloys Compd. 2021;865: 158836.

49. Wu J, Feng YJ, Logan BE, Dai CC, Han XY, Li D, Liu J. Preparation of Al-O-linked porous-g-C_3N_4/TiO_2-nanotube Z-scheme composites for efficient photocatalytic CO_2 conversion and 2,4-dichiorophenol decomposition and mechanism. ACS Sustain Chem Eng. 2019;7:15289.

50. Bohra D, Ledezma-Yanez I, Li GN, de Jong W, Pidko EA, Smith WA. Lateral adsorbate interactions inhibit HCOO- while promoting CO selectivity for CO_2 electrocatalysis on silver. Angew Chem Int Edit. 2019;58:1345.

51. Feaster JT, Shi C, Cave ER, Hatsukade TT, Abram DN, Kuhl KP, Hahn C, Norskov JK, Jaramillo TF. Understanding selectivity for the electrochemical reduction of carbon dioxide to formic acid and carbon monoxide on metal electrodes. ACS Catal. 2017;7:4822.

52. Li HX, Yue X, Qiu YS, Xiao Z, Yu XB, Xue C, Xiang JH. Selective electroreduction of CO_2 to formate over the co-electrodeposited Cu/Sn bimetallic catalyst. Mater Today Energy. 2021;21:100797.

53. Zhao ZL, Lu G. Computational screening of near-surface alloys for CO_2 electroreduction. ACS Catal. 2018;8:3885.

54. Ai CZ, Vegge T, Hansen HA. Metal-doped $PdH(111)$ catalysts for CO_2 reduction. Chemsuschem. 2022;15:e202200008.

55. Ju L, Tan X, Mao X, Gu YT, Smith S, Du AJ, Chen ZF, Chen CF, Kou LZ. Controllable CO_2 electrocatalytic reduction via ferroelectric switching on single atom anchored In_2Se_3 monolayer. Nat Commun. 2021;12:5128.

56. Guo L, Guo SB. Molecular transition metal corrole as an efficient electrocatalyst for the heterogeneous CO_2 electroreduction: a theory study. Int J Hydrog Energy. 2021;46:33120.

57. Wang S, Qian B, Wang Z, Yin B, Zheng YF, Ge L, Chen H, Yang H. High catalytic activity of Fe-based perovskite fuel electrode for direct CO_2 electroreduction in SOECs. J Alloys Compd. 2021;888:161573.

58. Zheng Y, Wang JC, Yu B, Zhang WQ, Chen J, Qiao JL, Zhang JJ. A review of high temperature co-electrolysis of H_2O and CO_2 to produce sustainable fuels using solid oxide electrolysis cells (SOECs): Advanced materials and technology. Chem Soc Rev. 2017;46:1427.

59. Tezel E, Guo DZ, Whitten A, Yarema G, Freire M, Denecke R, Mcewen JS, Nikolla E. Elucidating the role of B-site cations toward CO_2 reduction in perovskite-based solid oxide electrolysis cells. J Electrochem Soc. 2022;169:034532.

60. Bastidas DM, Tao SW, Irvine JTS. A symmetrical solid oxide fuel cell demonstrating redox stable perovskite electrodes. J Mater Chem. 2006;16:1603.

61. Jovanov ZP, Hansen HA, Varela AS, Malacrida P, Peterson AA, Norskov JK, Stephens IEL, Chorkendorff I. Opportunities and challenges in the electrocatalysis of CO_2 and CO reduction using bifunctional surfaces: a theoretical and experimental study of Au-Cd alloys. J Catal. 2016;343:215.

62. Lee JH, Kattel S, Jiang Z, Xie ZH, Yao SY, Tackett BM, Xu WQ, Marinkovic NS, Chen JGG. Tuning the activity and selectivity of electroreduction of CO_2 to synthesis gas using bimetallic catalysts. Nat Commun. 2019;10:3724.

63. Nian Y, Wang Y, Biswas AN, Chen XB, Han Y, Chen JGG. Trends and descriptors for tuning CO_2 electroreduction to synthesis gas over Ag and Au supported on transition metal carbides and nitrides. Chem Eng J. 2021;426:130781.

64. Samanta S, Srivastava R. Catalytic conversion of CO_2 to chemicals and fuels: the collective thermocatalytic/photocatalytic/electrocatalytic approach with graphitic carbon nitride. Mater Adv. 2020;1:1506.

65. Das S, Perez-Ramirez J, Gong JL, Dewangan N, Hidajat K, Gates BC, Kawi S. Core-shell structured catalysts for thermocatalytic, photocatalytic, and electrocatalytic conversion of CO_2. Chem Soc Rev. 2020;49:2937.

66. Alam MI, Cheula R, Moroni G, Nardi L, Maestri M. Mechanistic and multiscale aspects of thermo-catalytic CO_2 conversion to C_1 products. Catal Sci Technol. 2021;11:6601.

67. Jacot R, More R, Michalsky R, Steinfeld A, Patzke GR. Trends in the phase stability and thermochemical oxygen exchange of ceria doped with potentially tetravalent metals. J Mater Chem A. 2017;5:19901.

68. Muhich C, Hoes M, Steinfeld A. Mimicking tetravalent dopant behavior using paired charge compensating dopants to improve the redox performance of ceria for thermochemically splitting H_2O and CO_2. Acta Mater. 2018;144:728.

69. Gnanakumar ES, Chandran N, Kozhevnikov IV, Grau-Atienza A, Fernandez EVR, Sepulveda-Escribano A, Shiju NR. Highly efficient nickel-niobia composite catalysts for hydrogenation of CO_2 to methane. Chem Eng Sci. 2019;194:2.

70. Noh G, Lam E, Bregante DT, Meyet J, Sot P, Flaherty DW, Coperet C. Lewis acid strength of interfacial metal sites drives CH_3OH selectivity and formation rates on Cu-based CO_2 hydrogenation catalysts. Angew Chem Int Edit. 2021;60:9650.

71. Marcos FCF, Assaf JM, Assaf EM. Catalytic hydrogenation of CO_2 into methanol and dimethyl ether over Cu-X/V-Al PILC (X = Ce and Nb) catalysts. Catal Today. 2017;289:173.

72. Li QQ, Song LP, Liang Z, Sun MZ, Wu T, Huang BL, Luo F, Du YP, Yan CH. A review on CeO_2-based Electrocatalyst and photocatalyst in energy conversion. Adv Energy Sustain Res. 2021;2:2000063.

73. Damyanova S, Pawelec B, Arishtirova K, Huerta MVM, Fierro JLG. The effect of CeO_2 on the surface and catalytic properties of Pt/CeO_2-ZrO_2 catalysts for methane dry reforming. Appl Catal B. 2009;89:149.

74. Kaneko H, Taku S, Tamaura Y. Reduction reactivity of CeO_2-ZrO_2 oxide under high O_2 partial pressure in two-step water splitting process. Sol Energy. 2011;85:2321.

75. Zhang HY, Tian WJ, Li YG, Sun HQ, Tade MO, Wang SB. A comparative study of metal (Ni Co, or Mn)-borate catalysts and their photodeposition on rGO/ZnO nanoarrays for photoelectrochemical water splitting. J Mater Chem A. 2018;6:24149.

76. Jacot R, Naik JM, More R, Michalsky R, Steinfeld A, Patzke GR. Reactive stability of promising scalable doped ceria materials for thermochemical two-step CO_2 dissociation. J Mater Chem A. 2018;6:5807.